APPLIED GEOPHYSICS, Vol.21, No.4 (December 2024), P.805–819, 15 Figures.
DOI:10.1007/s11770-024-1142-3

Prediction of carbonate permeability from multi-resolution CT scans and deep learning

Zhang Lin[1], Chen Guang-dong[1], Ba Jing[1]*, José M. Carcione[1,2], Xu Wen-hao[1,3], and Fang Zhi-jian[1]

Abstract: The low-resolution CT scan images obtained from drill core generally struggle with problems such as insufficient pore structure information and incomplete image details. Consequently, predicting the permeability of heterogeneous reservoir cores relies heavily on high-resolution CT scanning images. However, this approach requires a considerable amount of data and is associated with high costs. To solve this problem, a method for predicting core permeability based on deep learning using CT scan images with different resolutions is proposed in this work. First, the high-resolution CT scans are preprocessed and then cubic subsets are extracted. The permeability of each subset is estimated using the Lattice Boltzmann Method (LBM) and forms the training set for the convolutional neural network (CNN) model. Subsequently, the high-resolution images are downsampled to obtain the low-resolution grayscale images. In the comparative analysis of the porosities of different low-resolution images, the low-resolution image with a resolution of 10% of the original image is considered as the test set in this paper. It is found that the permeabilities predicted from the low-resolution images are in good agreement with the values calculated by the LBM. In addition, the test data are compared with the results of the Kozeny-Carman (KC) model and the measured permeability of the whole sample. The results show that the prediction of the permeability of tight carbonate rock based on deep learning using CT scans with different resolutions is reliable.
Keywords: CT scans; deep learning; carbonate; permeability

Introduction

Permeability is a key parameter in the evaluation of high-quality underground reservoirs and is widely used in fields such as oil exploration and geological engineering. It indicates the ability of fluids to flow through porous media and its value is closely related to the pore structure of the medium (Doyen, 1988; Fredrich et al., 1993; Gholami et al., 2012; Karimpouli et al., 2010; Mohaghegh et al., 1995). Considering that the morphology, spatial distribution and connectivity of pores and cracks have a direct influence on the flowability of subsurface fluids in rocks, the accurate extraction of pore structure and the establishment of a quantitative relationship between pore structure and permeability are of great importance for optimizing reservoir development and improving the efficiency of resource utilization (Ba et al., 2023; Giesche, 2006; Katz et al., 1986; Rezaee et al., 2006; Ross and Bustin, 2009).

Manuscript received by the Editor August 22, 2024; revised manuscript received October 26th, 2024
1 School of Earth Science and Engineering, Hohai University, Nanjing 211100
2 National Institute of Oceanography and Applied Geophysics (OGS), Trieste, Italy 34010
3 BGP INC., China National Petroleum Corporation, Zhuozhou 072751, China
*Corresponding author: Ba Jing (Email: jba@hhu.edu.cn).

In recent years, the advancement of X-ray micro-computed tomography (micro-CT) has opened up new possibilities for the accurate extraction of the internal pore structure of rocks (Goral et al., 2019; Pang et al., 2024; Peng et al., 2012; Salek and Beckingham, 2023; Schmitt et al., 2016; Wildenschild et al., 2002; Zhai et al., 2020). Dehghan Khalili et al. (2013) provided a detailed characterization of pore structure in carbonate rocks using CT scans at different resolutions and discussed the applicability of the porosity-permeability relationship determined based on CT imaging on a large scale. Ramandi et al. (2016) developed a novel imaging agent technology that used CT scans to visualize internal fractures in coal rock and analyzed the effects of rock type and mineralization on the permeability of coal rock. Liu et al. (2017) combined micro-CT and SEM techniques to construct a digital multiscale core and characterize the pore structure of tight sandstone from the Yanchang Formation in the Ordos Basin, finding that the permeability and electrical conductivity of these sandstones are primarily dominated by micropores, with permeability being more dependent on pore structure than porosity. Huaimin Dong et al. (2023) integrated micro-CT images, nuclear magnetic resonance measurements, experimental mercury injection data, and fractal discrete fracture networks to creat a high-precision digital core of complex porous rocks. Zhu et al. (2024) used this technology to extract pore structures from coarse sandstones, medium sandstones and siltstoneand calculate the effective permeability of the three sandstone types using the Navier-Stokes equations. The investigations show that porosity and permeability generally have a linear relationship. However, at low porosity values, the data show considerable scatter, so that the consideration of pore structure parameters (e.g. pore throat radius) is necessary for a more accurate assessment of permeability. This technology not only reveals the microstructure of the porous medium, but also forms the basis for subsequent simulations of rock elasticity and transport properties (Amstan, 2019; Blunt et al., 2013; Chung et al., 2019; Pang et al., 2024; Wildenschild and Sheppard, 2013).

In CT imaging, the quality of reconstructed images is directly influenced by the field of view and image resolution, both of which are closely related to the number of voxels in each dimension (Sakellariou et al., 2004). Peng et al. (2014) found that the permeabilities predicted from two CT images, with resolutions of 1.85 μm/pixel and 5.92 μm/pixel for the Berea sandstone were almost identical. This result suggests that lower resolution images can capture the primary flow paths of the rock, while smaller pores can be neglected. Shah et al. (2015) discussed the effects of different voxel resolutions on the result of three-dimensional (3D) pore-scale imaging of different porous media. Although low-resolution images cover a wider range of samples and can effectively capture their heterogeneity, they are limited in their ability to accurately reflect small-scale pore structures, making them unsuitable for direct permeability calculations. In contrast, high-resolution images provide more detailed information about the pore structure and are suitable for the direct calculation of flow properties. However, their coverage area is smaller and often does not match the scale of core samples used in conventional experiments (Botha and Sheppard, 2016). Therefore, CT imaging needs to find a balance between resolution and field of view to ensure image quality while adequately representing the overall properties of the sample.

Neural networks are one of the cores of machine learning algorithms. Qadrouh et al. (2019) predict reservoir permeability from well logs data by using a neural network. Moreover, considering the significant advantages of deep learning in feature extraction and classification, it plays an important role in extracting detailed information from CT scan images. Alqahtani et al. (2018) proposed an innovative solution based on deep learning that utilizes a supervised learning method for fast prediction of various physical properties of porous media from two-dimensional (2D) micro-CT images using convolutional neural networks (CNNs). This method effectively addresses the loss of detail that occurs in conventional image segmentation techniques when processing smaller pore structures, as well as the discrepancies in results that can arise due to users' subjective biases. You et al. (2021) used a progressive growing generative adversarial network (PG-GAN) to obtain high-quality grayscale cross-sectional images, and applied linear interpolation to reconstruct full 3D digital cores from sparse 2D scans. They found that the reconstructed images and the extracted pore networks were visually almost identical to the real data, overcoming the limitations of conventional imaging technologies (such as micro-CT), including high costs and low resolution. This precise characterization of pore structures is crucial for simulating fluid flow paths in rocks and predicting the permeability of rock reservoirs (Blunt et al., 2013; Da Wang et al., 2019; Jiang et al., 2023; Ni et al., 2021; Shah et al., 2016). Martys et al. (1999) were the first to identify the resolution requirements necessary for permeability simulation, which typically require sufficiently high image resolution to accurately characterize the flow paths of pore systems with at least four open pixels. In particular, the pixel size must be at least four times smaller than the minimum throat diameter. The reason for this is that in simulations the interface between the solid and the fluid must fulfill the non-sliding condition: Of the four pixels, only the two middle open pixels allow significant flow. In lower resolution images, the throats may only be represented by grayscale pixels, rendering the simulation of fluid flow ineffective and leading to a predicted permeability of zero. Sudakov et al. (2018) systematically compared the performance of different machine learning and deep learning models in permeability prediction from images based on permeability simulated by 3D CT scan images of Berea sandstone and pore network methods.

Especially when simulating the permeability of reservoir rocks with the LBM, it is essential to solve the Navier-Stokes equations within high-resolution pore structures (Boek et al., 2010; Jiang et al., 2014; Raeini et al., 2012). Apourvari and Arns (2014) improved the LBM by incorporating the Brinkman approach (Brinkman, 1949) to evaluate the effects of sub-resolution porosity on permeability. Although this method accounts for regions of sub-resolution porosity, it still requires estimation of permeability in these areas where it is often challenging to determine the geometric morphology of the pore space a priori. Tembely et al. (2020) compared three numerical simulation techniques for calculating rock permeability based on high-resolution CT scan images:Pore Network Modeling (PNM), Finite Volume Method (FVM), and LBM. They proposed a machine learning process to quickly and accurately predict permeability from 3D micro-CT images. In 2021, they expanded this method to develop an artificial intelligence workflow to quickly estimate the permeability of complex carbonate rocks. Chung et al. (2021) introduced a novel analysis method - the concentric tube method - to study flow fields in low-resolution CT images with under-resolved features and found that the average error in permeability obtained from down-sampled images was 13.2% compared to the value derived from high-resolution images. Jiang et al. (2023) combined original CT image data of rocks with permeabilities obtained from LBM flow simulations with high-resolution CT images and trained a neural network with deep learning techniques to predict the permeability distribution in larger areas. Finally, they used a Darcy flow solver to calculate the permeability of the entire core, which led to results that closely matched the experimental data.

Considering that the simulation of rock permeability based on high-resolution CT scan images is accurate but time-consuming and inefficient, a deep learning method for predicting permeability using CT scan images with different resolutions is proposed in this study. Firstly, high-resolution CT scan images are processed and subsets are extracted, and the permeability of each subset is calculated using the LBM to generate the training data for the deep learning model. Subsequently, the high-resolution CT scan images are downsampled to varying degrees to determine a minimum acceptable resolution for the input data to ensure that computational accuracy is maintained. Finally, the generated deep learning model is used to predict rock permeability and the predicted results are compared with the measured values.

Rock samples

The MX-A dolomite sample used in this study was obtained from the carbonate reservoir of the Longwangmiao Formation in the Gao Shiti-Moxi area of the Sichuan Basin. Due to several episodes of tectonic movement and diagenetic processes, the reservoir exhibits characteristics such as strong heterogeneity, low porosity and permeability, and a variety of pore-fracture types (Zeng et al., 2014). The test sample was taken from a depth of 4656.7 m and is a cylindrical specimen with a length of 50.31 mm and a diameters of 37.93 mm. The measured dry density, porosity and permeability were 2.679 g/cm³, 3.52%, and 0.088 mD, respectively. The main technical specifications of the equipment used for the CT scanning experiments included a maximum X-ray source voltage of 120 keV, a resolution of 1-2 μm, and a sample size range of 2-50 mm. Figure 1 shows a selection of CT scan images of the sample, including ten representative CT images. The results show that the sample is tight, has fewer pores and poor connectivity.

During the CT scanning process, the sample was scanned at a high resolution of 27.6 μm/voxel, resulting in an image of 1430×1446 pixels. This configuration enables the capture of fine internal pore structures and their interconnection details within the sample. Figure

2 shows the pore structure of the sample after image segmentation, and illustrates that the pores and cracks (shown in black) occupy a relatively small portion of the sample and have low connectivity, which is consistent with the measured low porosity and permeability .

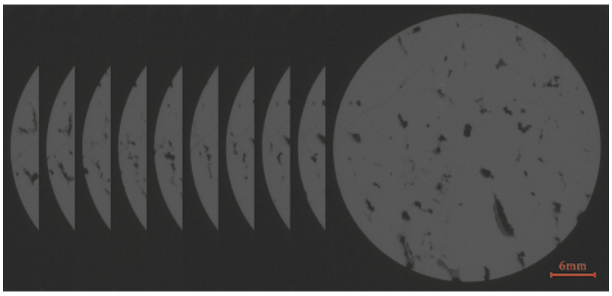

Figure 1. CT scan images.The figure displays a total of 10 images, starting from sample number N0320, with one image selected every 16 images, comprising 10 representative ones.

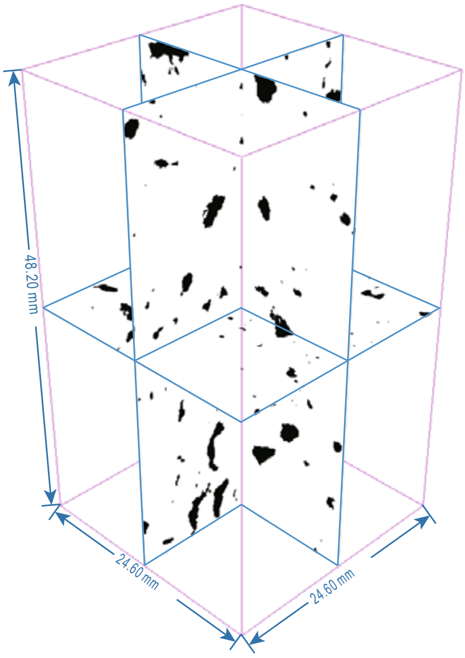

Figure 2. Pore structure of the rock sample after image segmentation.

Dataset Preparation

1. Training Dataset

1.1 Processing of CT Scan Data

In order to provide standardized training data for permeability prediction using deep learning with CT scan images of different resolutions, preprocessing, data selection and subset detection for the obtained high-resolution CT scan images were performed in this study to ensure data quality and applicability. The specific workflow is as follows:

a. CT image acquisition: A CT scanning device was used to scan a carbonate rock sample with a diameter of 37.93 mm at a resolution sof 27.6 μm/voxel, resulting in a total of 1971 CT scan images.

b. Image preprocessing: (1) Cropping: Images were cropped around the center of the scanned image to obtain square images with a resolution of 900×900 pixels (see Figure 3b). (2) Noise reduction: Since the acquired CT images were grayscale and contained significant noise, mean filtering was applied to improve the image quality. This filtering method effectively reduced the noise and producted smoother and more uniform images while preserving the boundary features, as shown in Figure 3c. (3) Threshold Segmentation: To convert the images into a binary format, a simple thresholding algorithm was used. This algorithm, which is based on the histogram, assigns labels according to voxel intensity. By selecting a local minimum of the intensity histogram as the threshold, a binary image was generated (Figure 3d), with a threshold value of 55 being selected.

c. Data Selection: From the 1971 images acquired, erroneous data from both ends were removed, resulting in a final data set of 1600 binary images and 1600 grayscale images, ensuring accuracy and reliability.

d. Subset Acquisition: The 900×900 pixel images were further segmented into subsets of 100 × 100 pixels. Each profile contained 81 sub-volumes with a depth of 16, resulting in a total of 1296 sub-volumes. The segmentation process is illustrated in Figure 4. Figure 5 shows the distribution of binary porosity across the different subsets, and clearly shows that most of the porosities of the subsets are in the range of 0-0.05, while the frequency distribution of porosity values between 0.1 and 0.2 is relatively uniform and generally higher. This observation indicates that the majority of the subset images show low porosity, but a certain number of samples still show high porosity. In the range of 0.3 to 0.4, the frequency of porosity values decreases significantly.

1.2 Calculation of Permeability for the Subset

The methods for calculating rock permeability based on CT scan images include PNM, FVM, LBM, etc (Zhang et al., 2021; Li et al., 2017). This study primarily employs the LBM to compute the permeability of the subset. The core of this approach is the discretized Boltzmann equation, which describes the evolution of the particle distribution function in both space and time,

$$f_i(\mathbf{x}+\mathbf{c}_i\Delta t, t+\Delta t) - f_i(\mathbf{x},t) = -\frac{1}{\tau}\left(f_i(\mathbf{x},t) - f_i^{eq}(\mathbf{x},t)\right), \tag{1}$$

where $f_i(\mathbf{x},t)$ represents the particle distribution function at position x and time t for particles with velocity $\mathbf{c}_i$. denoting discrete velocity directions (a 3D lattice with 19 velocity vectors (D3Q19) is used in the present study), Δt is the time step, τ is the relaxation time and f_i^{eq} is the equilibrium distribution function:

$$f_i^{eq} = \omega_i\rho\left(1+\frac{\mathbf{c}_i\cdot\mathbf{u}}{c_s^2}+\frac{(\mathbf{c}_i\cdot\mathbf{u})^2}{2c_s^4}-\frac{\mathbf{u}\cdot\mathbf{u}}{2c_s^2}\right), \tag{2}$$

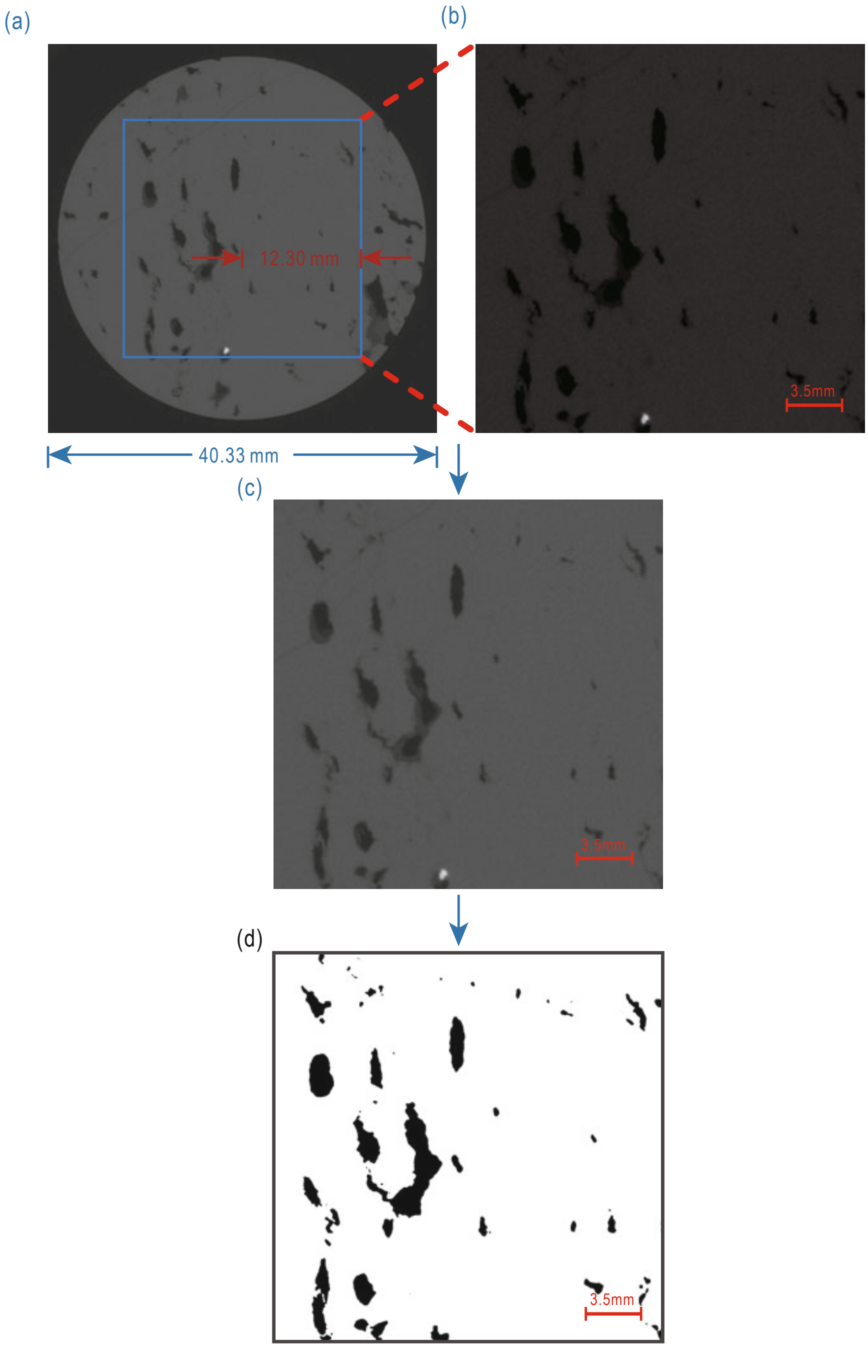

Figure 3. (a) Original grayscale image (1430 × 1446 pixels), (b) Cropped image (900 × 900 pixels), (c) Filtered image, (d) Binary pore image.

where ω_i represents the weight associated with the velocity $\mathbf{c}_i$. The lattice speed is denoted by c_s. The macroscopic density ρ and velocity $\mathbf{u}$ can be computed from the distribution function.

$$\rho = \sum_i f_i \ , \tag{3}$$

$$\rho\mathbf{u} = \sum_i f_i \mathbf{c}_i \ . \tag{4}$$

The steps involved in the lattice Boltzmann method (LBM) for calculating permeability are as follows: First, initialize the distribution function for the lattice points and the macroscopic variables, such as density (ρ) and velocity ($\mathbf{u}$). Next, the Bhatnagar-Gross-Krook (BGK) model is applied to compute the post-collision distribution function, which is then propagated to adjacent lattice points in the corresponding direction. During the propagation process, the solid walls, periodic boundaries, and inlet/outlet boundaries are typically handled using the rebound method. Subsequently, the macroscopic variables are recovered from the updated distribution function. This process is repeated to advance the simulation until the termination condition is met. The calculated subset permeability (shown in Figure 6) is utilized for deep learning training. The results indicate that most subset permeability values are concentrated in the range of 0-0.1 mD, while the frequency of values in the range of 0.1-0.5 mD is significantly lower, suggesting that most subsets exhibit low permeability.

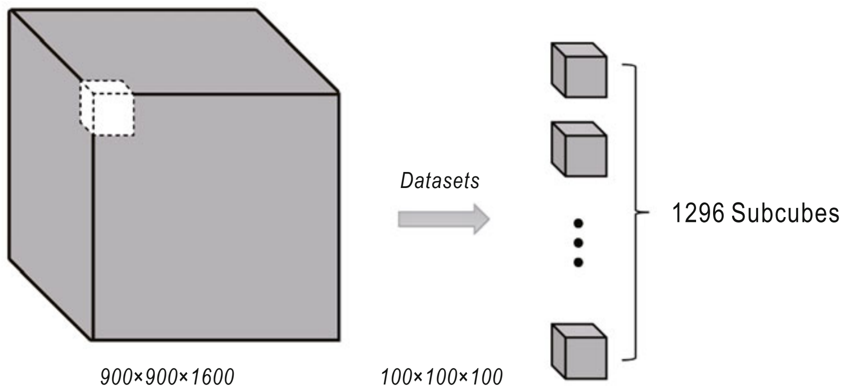

Figure 4. Dividing the 3D Rock Core into subset with 100×100×100 Dimensions.

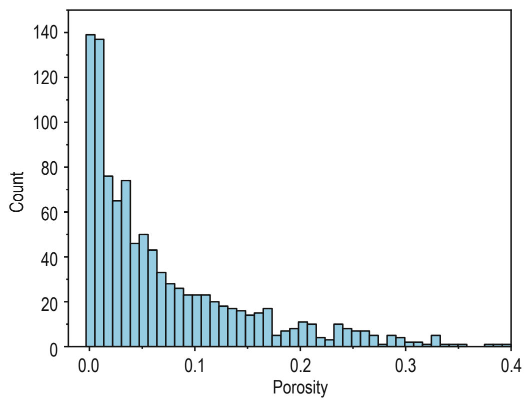

Figure 5. Histogram of porosity statistics of the subset.

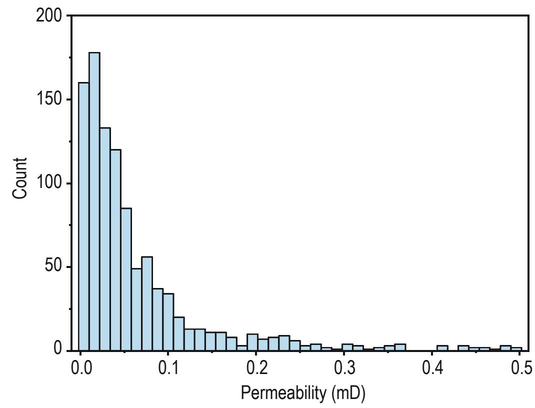

Figure 6 Histogram of permeability statistics of the subset.

2. Model Training

2.1 Convolutional Neural Networks

Convolutional Neural Networks (ConvNets) are essential components of deep learning models, designed to effectively extract features through a series of nonlinear transformations achieved by convolutional layers (Alqahtani et al., 2021; LeCun et al., 1998). This study employs a 3D Convolutional Neural Network (3D CNN) for permeability prediction, which is capable of extracting features across three spatial dimensions while thoroughly considering contextual information. This

3D feature extraction ability enables the CNN to better capture the complexities of rock microstructure when processing CT scan images. The architecture of the 3D CNN includes convolutional layers, pooling layers, and fully connected layers, as illustrated in Figure 7. This architecture includes an input layer, hidden layers, and an output layer.

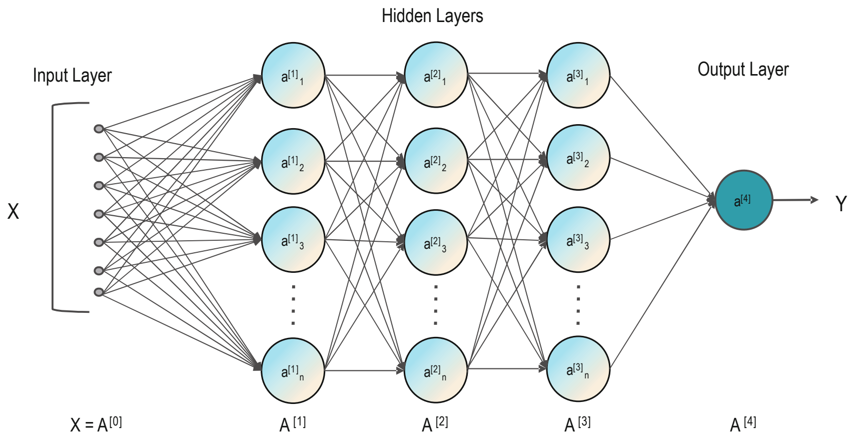

Figure 7. Schematic diagram of the Convolutional Neural Network.

ResNet, a deep residual network, primarily addresses the issues of vanishing and exploding gradients by introducing residual blocks during the construction of the CNN. This approach enables the network to be trained at greater depths, overcoming the performance limitations encountered by traditional CNN as their depth increases (He et al., 2016). The fundamental structure of ResNet comprises several key components:

a. Initial Convolutional Layer: ResNet typically begins with a 7×7 convolutional layer with a stride of 2, followed by a max pooling layer for preliminary feature extraction from the CT images of rock samples.

b. Residual Blocks: Central to ResNet are multiple residual blocks, each containing several convolutional layers. These blocks are connected through shortcut (or identity) connections, which directly link the input to the output of the convolutional layers. This design allows the network to retain important feature information during deep learning, enhancing training efficiency by minimizing information loss.

c. Global Average Pooling Layer: Following the residual blocks, ResNet utilizes a global average pooling layer instead of a traditional fully connected layer. This significantly reduces model parameters and mitigates the risk of overfitting.

d. Fully Connected Layer: Finally, the features obtained from global average pooling layer are input into a fully connected layer to produce the predicted permeability results.

The model selected for this study is ResNet-34, which comprises 34 layers, as shown in Figure 8. With its deeper network structure, ResNet-34 can effectively learn complex features in rock CT images. However, as the network depth increases, the demands for training time and computational resources also rise.

2.2 Loss Function and Accuracy Measurement

During the training process, five loss functions were employed to optimize the network model, namely: Mean Squared Error (MSE, see Equation 5), Mean Absolute Error (MAE, Equation 6), Huber Loss (Equation 7), Mean Squared Logarithmic Error (MSLE, Equation 8), and Log-Cosh Loss (Equation 9).

$$\frac{1}{n}\sum_{j=1}^{n}\left(y_j - y_j^p\right)^2, \tag{5}$$

$$\frac{1}{n}\sum_{j=1}^{n}|y_j - y_j^p|, \tag{6}$$

$$\begin{cases} \frac{1}{n}\sum_{j=1}^{n}\frac{1}{2}\left(y_j - y_j^p\right)^2, if\ |y_j - y_j^p| \le \delta \\ \frac{1}{n}\sum_{j=1}^{n}\delta\times\left(|y_j - y_j^p| - \frac{1}{2}\delta\right), if\ |y_j - y_j^p| > \delta \end{cases}, \tag{7}$$

$$\frac{1}{n}\sum_{j=1}^{n}\left(\log(y_j+1) - \log(y_j^p+1)\right)^2, \tag{8}$$

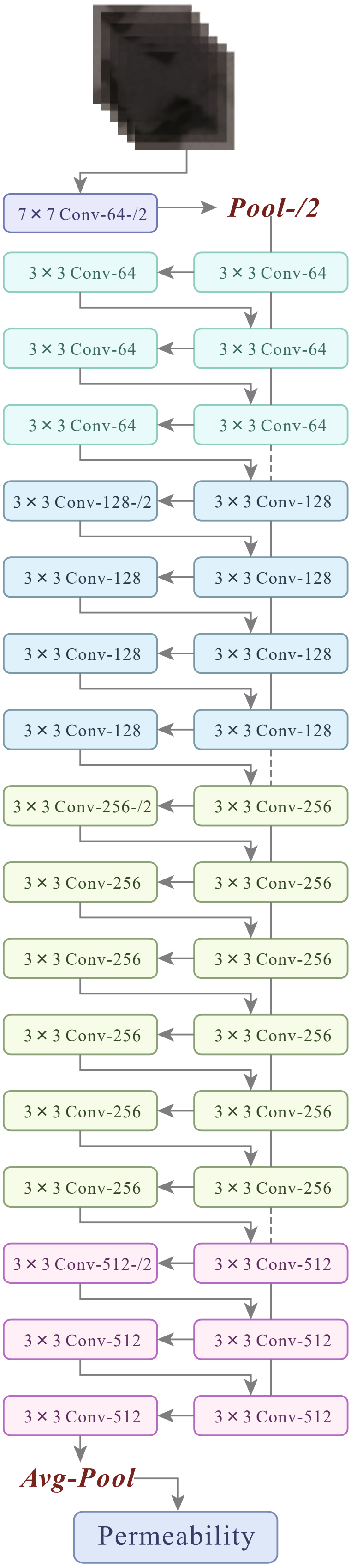

Figure 8. Structure of the ResNet-34 Residual Neural Network.

$$\frac{1}{n}\sum_{j=1}^{n}\log\Big(\frac{\exp(y_j^p - y_j) - \exp(y_j - y_j^p)}{2}\Big). \quad (9)$$

where y_j represents the actual value of the j-th sample, the superscript p denotes the predicted value, and n indicates the number of samples in each dataset.

Predicting penetration rates based on multi-resolution CT scans

1. Multi-resolution CT scan images

In this study, a linear interpolation method is used to downsample 1600 high-resolution grayscale images to obtain lower-resolution counterparts. Figure 9 shows the comparison between the downsampled image and the original image. The number 90×90 in the figure indicates that the resolution of the image was reduced to 10% of the original image, with the file size dropping from 364 KB to 5.24 KB. It can be seen that the details of the pore structure in the images gradually become blurred as the resolution decreases. To further analyze the effect of resolution on the pore structure, three images with different resolutions- 920 μm/voxel, 276 μm/voxel and 27.6 μm/voxel-were selected as low, medium, and high-resolution grayscale images. These included 2D slices of the selected regions, grayscale histograms and intensity distribution analyses, the results of which are shown in Figure 10. As the image resolution decreases, the intensity distribution shows significant smoothing and the smaller details of the pore structure are difficult to captured adequately. This phenomenon is particularly noticeable in the lower resolution images. In addition, images with a resolution of 920 μm/voxel show a general increase in the mean gray values in the intensity histogram due to spatial averaging (i.e., blurring effect). This behavior results in multiple regions of the pore space, especially the pore throat part, being characterized by a large number of intermediate gray values, thus compromising the accurate identification and characterization of these key features.

The porosities of 1600 grayscale images were then calculated under different resolutions, as shown in Figure 11. The results show that at a resolution of more than 276 μm/voxel, the porosities derived from low-resolution images closely match the porosities calculated from high-resolution images, with only minimal differences between the values. However, when the resolution is below 276 μm/voxel, significant deviations in porosity trends between low- and high-resolution images are evident, with porosity values from low-resolution images generally falling below those predicted from high-resolution images. This

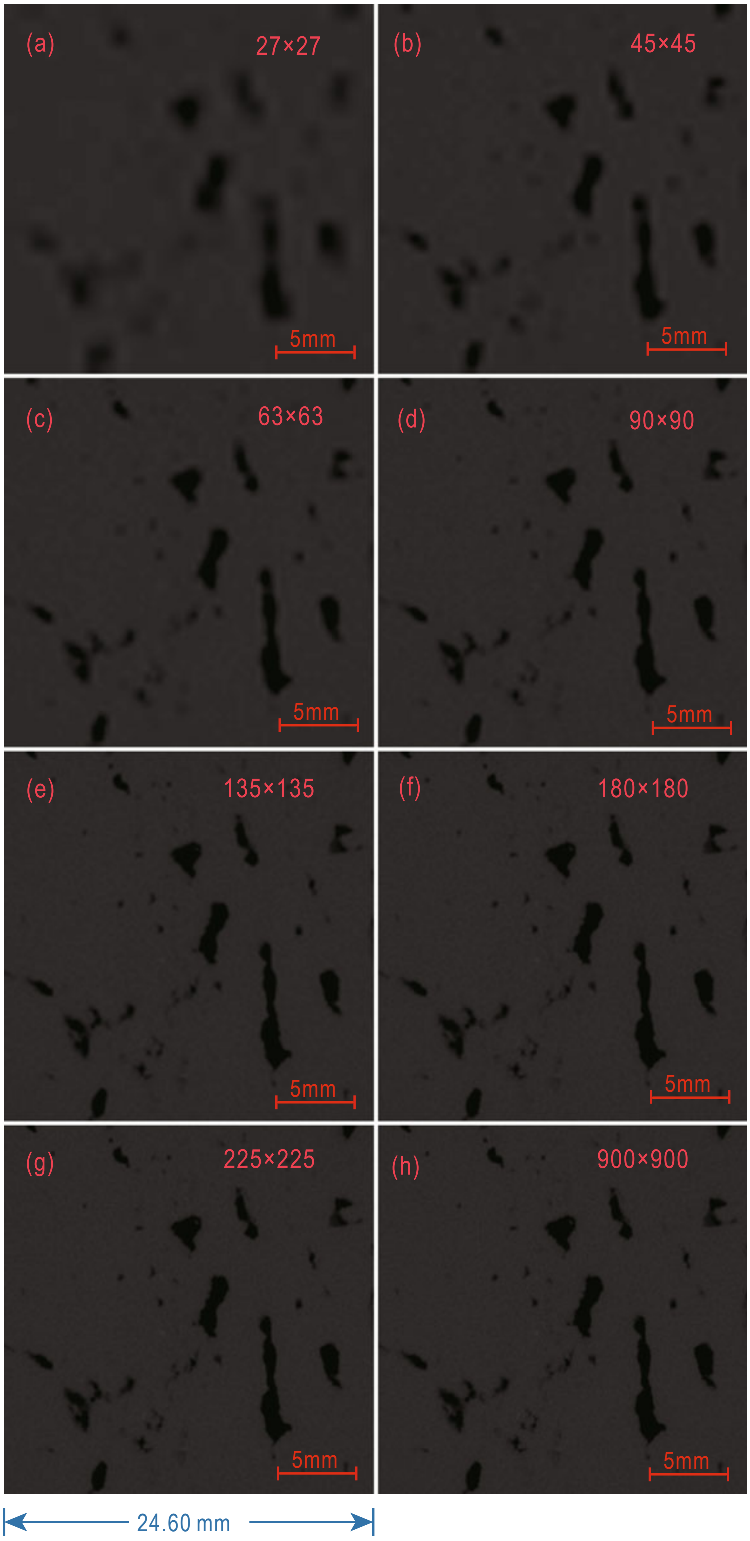

Figure 9 Comparison of grayscale images with different resolutions. (a) 920μm/voxel, (b) 552μm/voxel, (c) 394.3μm/voxel, (d) 276μm/voxel, (e) 184μm/voxel, (f) 138μm/voxel, (g) 110.4μm/voxel, (h) 27.6μm/voxel

phenomenon suggests that porosity within a given range can be effectively calculated from low-resolution images, saving significant computational time and allowing large amounts of image data to be processed on smaller computers. Error analysis of the data (as shown in Figure 12) show that the error value decreases with increasing resolution. Specifically, at a resolution of 276 μm/voxel, the error value approaches zero, which further

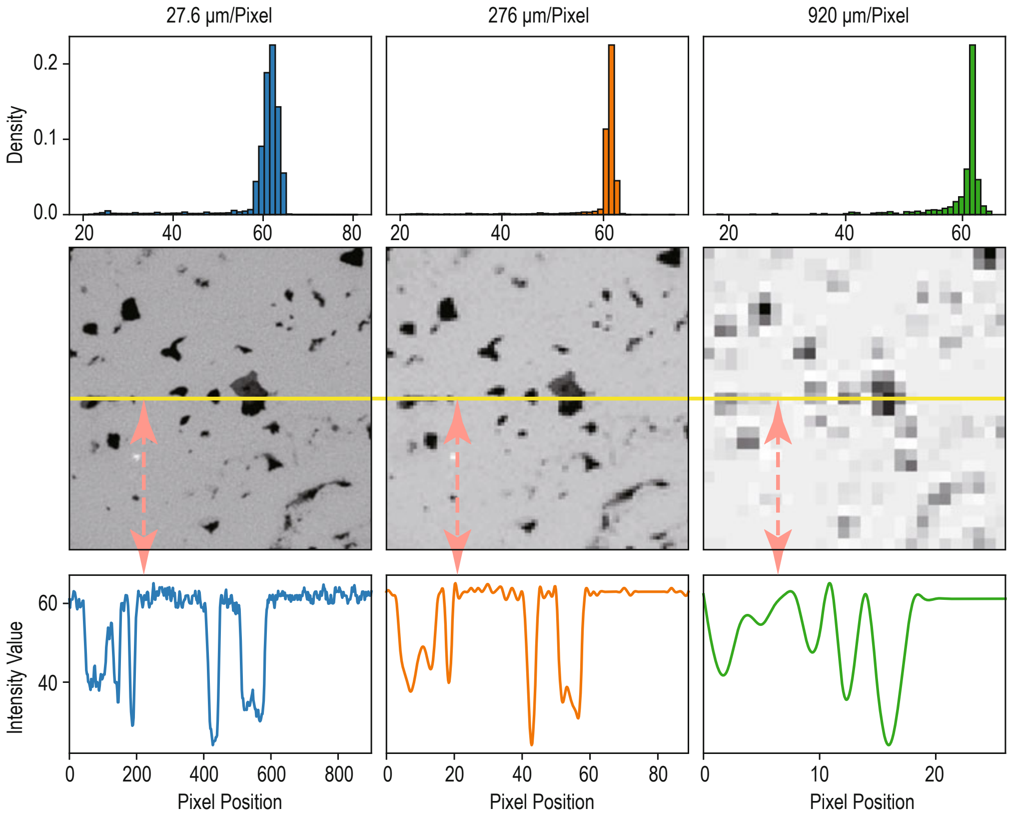

Figure 10. Close-up areas captured in three different resolutions of grayscale images. (a) 27.6 μm/voxel, (b) I276 μm/voxel, (c) 920 μm/voxel. Each image is accompanied by a grayscale histogram above and an intensity distribution below, with the position indicated by a yellow line.

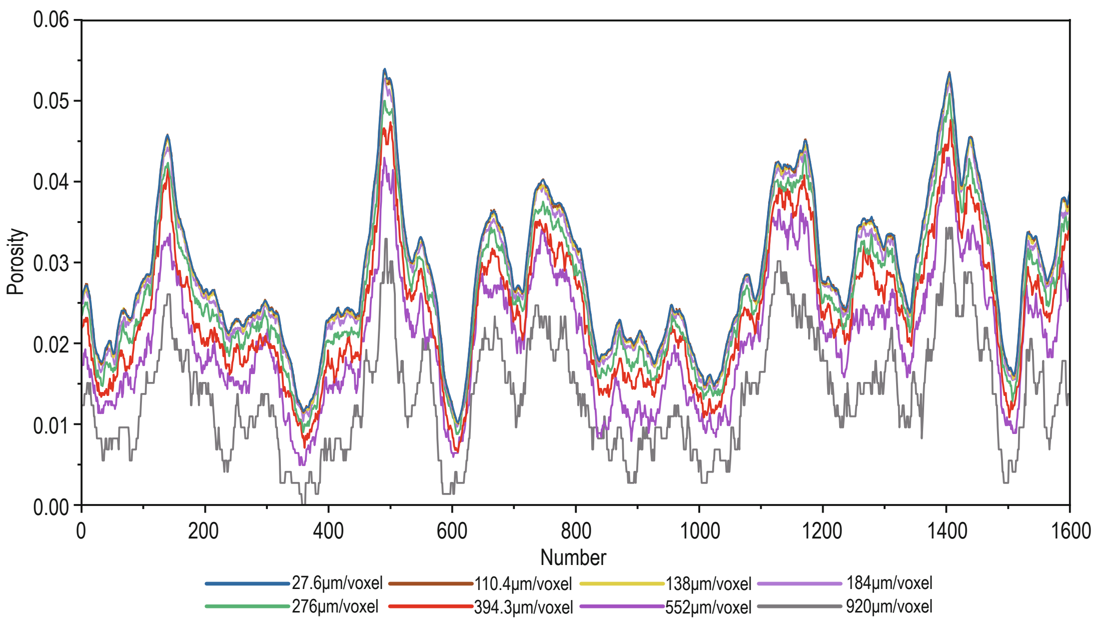

Figure 11. Corresponding Porosity of 1600 Grayscale Images with Different Resolutions.

confirms the above conclusions. Consequently, images with a resolution of 276 μm/voxel were selected as the input data for the subsequent deep learning model. This choice not only enhances computational efficiency, but also ensures the data quality required for model training, providing a reliable foundation for future estimates of rock permeability.

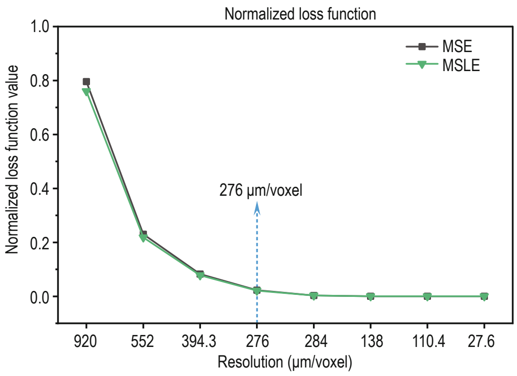

Figure 12. Normalized Error Functions for Porosity of Images with Different Resolutions.

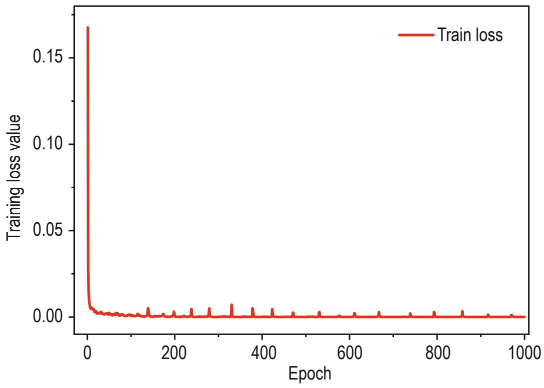

Figure 13. Loss Function for Permeability Prediction.

is performing suboptimally in the initial data fitting and still has much room for improvement. As training progresses, the decrease in the loss value gradually slows down, indicating that the model is approaching an optimal state and that the training results are becoming more stable.

Figure 14 presents a comparison between the predicted results of the model and the actual calculated results on the test set. The results show that the predicted values are largely consistent with the trends of the actual permeability calculations, and the numerical

2. Permeability Prediction

2.1 Subset Permeability of Lower Resolution Images

Similar to Section 3.1, this study processes lower-resolution CT scan images to obtain the permeability of each subset, using these images as the test set for the deep learning model designed for the predict. The learning rate is set to 0.001, and the Adam optimizer is utilized for 1,000 iterations on a training platform equipped with 64 GB RAM and an NVIDIA RTX 1650S GPU. MSE is employed as the loss function to quantify the difference between the model's predicted values and the actual labels.

Figure 13 shows the the development of the loss function during the training process. It is noticeable that the total loss value decreases with training, indicating that the model is progressively learning and effectively capturing the data features, improving its predictive ability. In the early stages of training, the loss value decreases rapidly, suggesting that the model

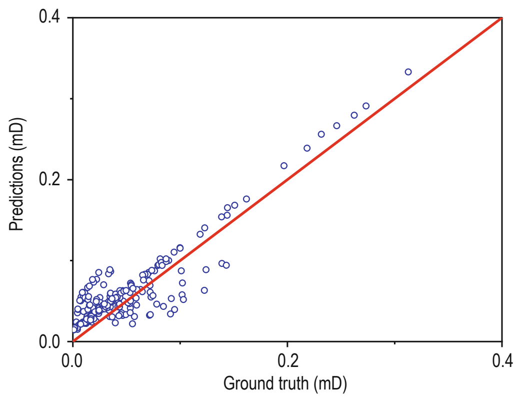

Figure 14. Crossplot of Calculated Data (Ground Truth) and Predicted Results from Test Data.

values are also very consistent. Table 1 shows the values of the different error functions for the test set. With the exception of the MSE, the values of the other loss functions are all less than 1, with the MAE being only 0.740098. This indicates that the prediction performance for the samples of the permeability test set is excellent. These results show that effective data augmentation and optimization of the model architecture significantly improve both prediction accuracy and stability.

Table 1. Values of Various Error Functions for the Permeability Prediction Test Set.

Error Function	MSE	MAE	Huber	MSLE	Logcosh
Error	1.935215	0.740098	0.460062	0.241644	0.428651

2.2 Model verification

Previous studies have demonstrated a strong correlation between rock permeability and porosity. The most widely employed empirical relationship between permeability and porosity is described by the Kozeny-Carman (KC) model (Carman, 1937):

$$K = C\frac{\phi^3}{(1-\phi)^2}, \tag{10}$$

where C is a parameter related to the geometric properties of the rock and ϕ denotes the porosity. The empirical parameter C in the model is typically not constant and is challenging to determine (Xu and Yu, 2008). To further assess the prediction performance of the deep learning model in this study, we compared its test data with the results obtained from the KC model. The comparison is shown in Fig. 15, The least squares method is used to apply the KC model to the computational dataset, yielding a C value of 0.01. In comparison to the predictions from the classical KC empirical model, the CNN prediction method in this study captures permeability change features with greater detail, especially when the effect of microstructural features is considered. Furthermore, this study utilizes a downsampled CT scan image as input to the deep learning model to predict the permeability of the entire rock sample, resulting in a prediction of 0.0775 mD, which is closer to the experimentally measured value of 0.088 mD. This indicates that the ResNet34 model has been effectively trained for permeability prediction, demonstrating high accuracy.

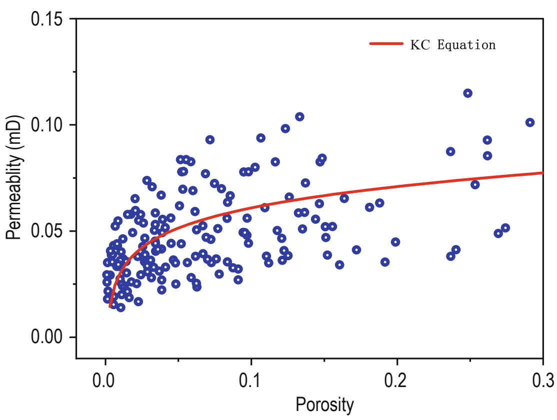

Figure 15. Relationship between permeability and porosity of the samples, the solid line indicates the result of KC equation curve fitting.

Conclusion

This study presents a method for predicting rock permeability based on deep learning using CT scan images with different resolutions. A training set of high-resolution CT scan images with the corresponding permeability values was created. Lower-resolution images, specifically those with a resolution of 276 μm/voxel, were used as the test set. The analysis shows that the test results closely match the permeability distributions calculated with the LBM. In addition, the predictions of the model were compared with those of the empirical Kozeny-Carman model and measured values. The comparisons show that the established deep learning model is effective for predicting permeability in tight carbonate rocks. This method not only reduces the cost and increase the efficiency of the calculations, but also utilizes the flexibility and scalability of deep learning approaches to account for variations in sample characteristics. If the types of samples and scanning conditions change, the required image resolution can also be adjusted accordingly. By using a deep learning model, the image processing workflow can be dynamically optimized based on specific sample characteristics, thereby improving the accuracy and reliability of permeability predictions in rock reservoirs.

Acknowledgments

This research was jointly funded by the National Natural Science Foundation of China (42104110, 42174161, 12334019, 42404120), the Jiangsu Natural Science Foundation (BK20210379), and the China Postdoctoral Science Foundation (2022M720989).

References

Alqahtani, N. J., Chung, T., Wang, Y. D., Armstrong, R. T., Swietojanski, P., & Mostaghimi, P., 2021, Flow-based characterization of digital rock images using deep learning: SPE Journal, **26**(4), 1800–1811.

Alqahtani, N., Armstrong, R. T., & Mostaghimi, P., 2018, Deep learning convolutional neural networks to predict porous media properties. SPE Asia Pacific oil and gas conference and exhibition (p.

D012S032R010). SPE.

Apourvari, S. N., and C. H. Arns., 2014, An assessment of the influence of micro-porosity for effective permeability using local flux analysis on tomographic images: Society of Petroleum Engineers - International Petroleum Technology Conference 2014, IPTC 2014, Unlocking Energy Through Innovation, Technology and Capability, pp. 2049–2058.

Armstrong R. T., McClure J. E., Robins V., et al., 2019, Porous media characterization using Minkowski functionals: Theories, applications and future directions: Transport in Porous Media, **130**, 305–335.

Arns, C. H., Knackstedt, M. A., Pinczewski, W. V., & Martys, N. S., 2004, Virtual permeametry on microtomographic images: Journal of Petroleum Science and Engineering, **45**(1–2), 41–46.

Ba, J., Zhu, H., Zhang, L., & Carcione, J. M., 2023, Effect of multiscale cracks on seismic wave propagation in tight sandstones: Journal of Geophysical Research: Solid Earth, **128**(10), e2023JB027474.

Blunt, M. J., Bijeljic, B., Dong, H., Gharbi, O., Iglauer, S., Mostaghimi, P., ... & Pentland, C., 2013, Pore-scale imaging and modelling: Advances in Water resources, **51**, 197–216.

Boek, E. S., & Venturoli, M., 2010, Lattice-Boltzmann studies of fluid flow in porous media with realistic rock geometries: Computers & Mathematics with Applications, **59**(7), 2305–2314.

Botchkarev, A., 2018, Performance metrics (error measures) in machine learning regression, forecasting and prognostics: Properties and typology. arXiv preprint arXiv:1809.03006.

Botha P W S K, Sheppard A P., 2016, Mapping permeability in low-resolution micro-CT images: A multiscale statistical approach: Water Resources Research, **52**(6), 4377–4398.

Brinkman, H. C., 1949, A calculation of the viscous force exerted by a flowing fluid on a dense swarm of particles: Applied Scientific Research, **1**(1), 27–34.

Carman, P. C., 1937, Fluid flow through granular beds: Transactions of the Institution of Chemical Engineers, **15**, 150–166.

Chung T, Wang Y D, Armstrong R T, et al., 2019, Approximating permeability of microcomputed-tomography images using elliptic flow equations: SPE Journal, **24**(03), 1154–1163.

Chung, T., Da Wang, Y., Armstrong, R. T., & Mostaghimi, P., 2021, Minimising the impact of sub-resolution features on fluid flow simulation in porous media: Journal of Petroleum Science and Engineering, 207, 109055.

Costa, A., 2006, Permeability-porosity relationship: A reexamination of the Kozeny-Carman equation based on a fractal pore-space geometry assumption: Geophysical Research Letters, **33**, L02318.

Da Wang, Y., Chung, T., Armstrong, R. T., McClure, J. E., & Mostaghimi, P., 2019, Computations of permeability of large rock images by dual grid domain decomposition: Advances in water resources, **126**, 1–14.

dos Anjos, C. E. M., de Matos, T. F., Avila, M. R. V., Fernandes, J. D. C. V., Surmas, R., & Evsukoff, A. G., 2023, Permeability estimation on raw micro-CT of carbonate rock samples using deep learning: Geoenergy Science and Engineering, **222**, 211335.

Fan, C., Jiang, X., Fan, N., Xiao, B., Yang, L., & Yang, Z., 2024, Scale Effect of Coal Porosity and Permeability Characteristics Based on CT 3D Reconstruction from a Microperspective: Energy & Fuels, **38**(3), 1813–1821.

Ferréol, B., and D. H. Rothman., 1995, Lattice-Boltzmann simulations of flow through Fontainebleau sandstone, in Multiphase Flow in Porous Media, edited by P. M. Adler, pp. 3–20, Springer, Netherlands.

Gholami R., Shahraki A. R., Jamali Paghaleh M., 2012, Prediction of hydrocarbon reservoirs permeability using support vector machine: Mathematical Problems in Engineering. 2012: 670723.

Giesche, H., 2006, Mercury Porosimetry: A General (Practical) Overview. Particle & Particle Systems Characterization, **23**(1): 9–19.

He, K., Zhang, X., Ren, S., & Sun, J., 2016, Deep residual learning for image recognition. In Proceedings of the IEEE conference on computer vision and pattern recognition (pp. 770–778). IEEE.

Huber, P. J., 1992, Robust estimation of a location parameter. In Breakthroughs in statistics (pp. 492–518). Springer.

Jiang F, Guo Y, Tsuji T, et al., 2023, Upscaling permeability using multiscale X-Ray-CT images with Digital rock modeling and Deep learning techniques: Water Resources Research, **59**(3), e2022WR033267.

Karimpouli S., Fathianpour N., Roohi J., 2010, A new approach to improve neural networks' algorithm in permeability prediction of petroleum reservoirs: Journal of Petroleum Science and Engineering, 73(3–4), 227–232.

Katz, A. J., Thompson, A. H., 1986, Quantitative Prediction of Permeability in Porous Rock. Physical Review B, **34**(11): 8179–8181.

LeCun, Y., Bottou, L., Bengio, Y., & Haffner, P., 1998, Gradient-based learning applied to document recognition. Proceedings of the IEEE, **86**(11), 2278–2324.

Li Ang, Yu Haobo, Xie Bin, Huang Bo, Feng Yaorong, Gong Jing, Hao Pengfei., 2017, Flow and Heat Transfer Study on Reconstructed Digital Core of Tight Oil Reservoir Based on FVM: Well Logging Technology, **41**(2), 135–140.

Liu, S. G., Yang, Y., Deng, B., et al., 2020, Tectonic Evolution of the Sichuan Basin, Southwest China: Earth-Science Reviews, **213**, 103470.

Liu, X., Wang, J., Ge, L., Hu, F., Li, C., Li, X., ... & Xue, Q., 2017, Pore-scale characterization of tight sandstone in Yanchang Formation Ordos Basin China using micro-CT and SEM imaging from nm-to cm-scale: Fuel, **209**, 254–264.

Martys, N. S., J. G. Hagedorn, D. Goujon, and J. E. Devaney., 1999, Large-scale simulations of single- and multicomponent flow in porous media, vol. 3772, in Proceedings of the SPIE - International Society for Optical Engineering, pp. 205–213, Denver, Colo.

Mohaghegh S., Arefi R., Ameri S., Rose D., 1995, Design and development of an artificial neural network for estimation of formation permeability: SPE Computer Applications, **7**(06), 151–154.

Ni, H., Liu, J., Huang, B., Pu, H., Meng, Q., Wang, Y., & Sha, Z., 2021, Quantitative analysis of pore structure and permeability characteristics of sandstone using SEM and CT images: Journal of Natural Gas Science and Engineering, **88**, 103861.

Peng, S., Hu, Q., Dultz, S., & Zhang, M., 2012, Using X-ray computed tomography in pore structure characterization for a Berea sandstone: Resolution effect: Journal of hydrology, **472**, 254–261.

Peng, S., F. Marone, and S. Dultz., 2014, Resolution effect in X-ray microcomputed tomography imaging and small pore's contribution to permeability for a Berea sandstone: Journal of Hydrology, **510**, 403–411.

Ramandi, H. L., Mostaghimi, P., Armstrong, R. T., Saadatfar, M., & Pinczewski, W. V., 2016, Porosity and permeability characterization of coal: a micro-computed tomography study: International Journal of Coal Geology, **154**, 57–68.

Rezaee, M. R., Jafari, A., Kazemzadeh, E., 2006, Relationships between Permeability, Porosity and Pore Throat Size in Carbonate Rocks Using Regression Analysis and Neural Networks: Journal of Geophysics and Engineering, **3**(4): 370–376.

Ross, D. J. K., Bustin, R. M., 2009, The Importance of Shale Composition and Pore Structure upon Gas Storage Potential of Shale Gas Reservoirs: Marine and Petroleum Geology, **26**(6): 916–927.

Sakellariou, A., T. J. Sawkins, T. J. Senden, and A. Limaye., 2004, X-ray tomography for mesoscale physics applications: Physica A, **339**(1–2), 152–158.

Salek, M. F., & Beckingham, L. E., 2023, Effect of X-Ray Computed Tomography Imaging Parameters on Quantification of Petrophysical Properties: Earth and Space Science, **10**(10), e2023EA003095.

Schmitt, M., Halisch, M., Müller, C., & Fernandes, C. P., 2015, Classification and quantification of pore shapes in sandstone reservoir rocks with 3-D X-ray micro-computed tomography: Solid Earth Discussions, **7**(4).

Sudakov, O., Burnaev, E., & Koroteev, D., 2019, Driving digital rock towards machine learning: Predicting permeability with gradient boosting and deep neural networks: Computers & geosciences, **127**, 91–98.

Wildenschild D, Sheppard A P., 2013, X-ray imaging and analysis techniques for quantifying pore-scale structure and processes in subsurface porous medium systems: Advances in Water resources, **51**, 217–246.

Wildenschild, D., Vaz, C. M. P., Rivers, M. L., Rikard, D., & Christensen, B. S. B., 2002, Using X-ray computed tomography in hydrology: systems, resolutions, and limitations: Journal of Hydrology, **267**(3-4), 285–297.

Xu, P., & Yu, B., 2008, Developing a new form of permeability and Kozeny-Carman constant for homogeneous porous media by means of fractal geometry: Advances in Water Resources, **31**(1), 74–81.

You, N., Li, Y. E., & Cheng, A., 2021, 3D carbonate digital rock reconstruction using progressive growing GAN: Journal of Geophysical Research: Solid Earth, 126(5), e2021JB021687.

Zeng Hongliu, Zhao Wenzhi, Xu Zhaohui, Fu Qilong, Hu Suyun, Wang Zecheng, Li Bohua., 2018, Carbonate seismic sedimentology: A case study of Cambrian Longwangmiao Formation, Gaoshiti-Moxi area, Sichuan Basin, China: Petroleum Exploration and Development, 2018, **45**(5): 775–784.

Zhang, D., R. Zhang, S. Chen, and W. E. Soll., 2000, Pore scale study of flow in porous media: Scale dependency, REV, and statistical REV: Geophysical Research Letters, **27**(8), 1195–1198.

Zhang, H., Abderrahmane, H., Al Kobaisi, M., & Sassi, M., 2021, Pore-scale characterization and pnm simulations of multiphase flow in carbonate rocks: Energies, **14**(21), 6897.

Zhang Lin received his Ph.D. degree in Exploration Geophysics from Hohai University in 2020, and is working as a associate professor in the School of Earth Sciences and Engineering, Hohai University, since 2020. His research interests are the elastic wave propagation theories of porous media and pore microstructure characterization.